

## Characteristics of flow around open channel 90° bends with vanes

Han<sup>1</sup>, S.S, Ramamurthy<sup>2</sup>, A.S. and Biron<sup>3</sup>, P.M.

**Abstract:** Sharp open channel bends are commonly encountered in hydraulic engineering design. Disturbances such as secondary flows and flow separation caused by the bend may persist for considerable distances in the downstream channel. A simple way of reducing these disturbances is through the insertion of vertical vanes in the bend section. A Laser Doppler Anemometry (LDA) unit was used to measure the three-dimensional mean and turbulent velocity components of flow in an experimental rectangular open channel bend. Flow characteristics of the bend with no vane are compared with those of bends having 1 or 3 vertical vanes. The size of the flow separation zone at the inner wall of the bend was determined from dye visualization data and confirmed using the mean streamwise velocity data. Results show that the vertical vanes are effective in considerably reducing flow separation, intensity of secondary flows and turbulence energy in the downstream channel. Furthermore, energy loss for bends with vanes is slightly less than for the no-vane case.

**Keywords:** Secondary flows; Flow separation; Vertical vanes; Laser Doppler anemometry; Turbulent kinetic energy; Bend induced energy loss

---

<sup>1</sup> Research Asst., Dept. of Building, Civil and Environmental Engineering, Concordia Univ., 1455 De Maisonneuve Blvd. W., Montreal, PQ, Canada H3G 1M8.<hansangsoo@gmail.com>

<sup>2</sup> Professor, Dept. of Building, Civil and Environmental Engineering, Concordia Univ., Montreal

<sup>3</sup> Assoc. Professor, Dept. of Geography, Planning and Environment, Concordia Univ., Montreal

## Introduction

Flow in open channel bends is commonly encountered in natural and artificial channel systems in hydraulic design practice. It is characterised by flow separation, secondary flows, energy losses and water surface variations caused by the bend curvature. Many earlier bend flow studies (Shukry 1949; Rozovskii 1957; Ippen & Drinker 1962; Kalkwijk and de Vriend 1980; De Vriend 1981; Dietrich and Smith 1983; Odgaard 1989a,b; Blanckaert and Graf 2001) provided only one- or two-dimensional mean velocity measurements with a relatively coarse spatial resolution, and they were often obtained in the central portion of the flow. Flow structures near the zone of flow separation and the secondary flow cell in the bend produce highly complex three-dimensional (3D) flow patterns which would be difficult to describe without the help of 3D velocity measurements. Recent velocity measurement methods such as the acoustic Doppler velocity profiler (ADVP) and laser Doppler anemometry (LDA) yield detailed 3D velocity data on a finer grid to identify flow characteristics like counter rotating secondary flow cells in open channel bends (Reinauer and Hager 1997; Tominaga et al. 1999; Tominaga and Nagao 2000; Blanckaert and Graf 2001; Booij 2003; Blanckaert and Lemmin 2006; Blanckaert 2009). Methods such as particle image velocimetry (PIV) are also increasingly used to get the detailed turbulent flow structure in complex flow fields (Ishigaki et al. 2002; Hyun et al. 2003; Sanjou and Nezu 2009).

In previous open channel bend studies (Shukry 1949; Rozovski 1957; De Vriend 1977; Booij 2003; Blanckaert and De Vriend 2004), considerable attention was devoted to secondary flow characteristics, without much emphasis on the flow separation that has broad and significant consequences for flows in bends of irrigation channels and natural meandering rivers. Various successful attempts were made in the past to counteract secondary currents using bendway weirs

(Przedwojski et al. 1995; Jia et al. 2005; Abad et al. 2008), outer bank footings (Roca et al. 2007), and submerged vanes (Odgaard and Kennedy 1983; Odgaard and Spoljaric 1986, 1989; Odgaard and Wang 1991a,b; Derrick et al. 1994). Bendway weirs, also known as rock vanes, spur dikes, groynes or jetties, have been used for decades to reduce erosion in river bends. These appurtenances deflect the near-bed high velocity flow away from the outer bank and disrupt the main secondary flow (Thornton et al. 2005). For bend flows, Odgaard and Wang (1991a,b) installed submerged vanes which are small, slender, airfoil shaped vanes. These were shown to generate secondary currents that modify near-bed flow patterns, reduce channel erosion, and also redistribute flow and sediment transport. Continuous vertical vanes, also called guide vanes, are widely adopted in water and wind tunnels to limit bend energy losses and obtain a very uniform flow at the straight section downstream of the bend (Barlow et al. 1999; Sahlin & Johansson 1991; Wetzal and Arndt 1994; Luo and Razinski 2009). With an appropriate design of such vanes, it is conceivable that flow separation, secondary flow and energy loss can also be reduced in an open channel bend, besides obtaining a more uniform flow in the channel downstream of the bend.

In engineering design of curved channels of width  $B$  and radius  $R$ ,  $B/R$  has to be limited to at least 0.33 to avoid secondary flows and flow separation (US Army Corps of Engineers 1994), although lower  $B/R$  values result in higher construction costs. Sharp bends for which  $B/R$  exceeds 0.33 are not avoidable in practice in irrigation channels. However, very few investigators in the past (Blanckaert 2009, Roca et al. 2009) have studied the role of secondary flows and turbulence energy on erosion especially in sharp bend flow.

The objectives of the present study are to advance the understanding of the complex three-dimensional flow structure around a sharp  $90^\circ$  bend and to assess the effectiveness of

continuous vertical vanes in reducing flow separation and secondary flows. Specifically, flow characteristics such as flow separation, secondary flows, turbulence energy, water surface fluctuations and energy loss in sharp bends with and without vanes are examined.

## Experimental Apparatus and Procedure

The experimental layout is shown schematically in Fig. 1a. A  $90^\circ$  sharp bend is connected to upstream (u/s) and downstream (d/s) rectangular channels with a horizontal bed of width  $B = 0.61\text{m}$ . The bend has an inner radius  $R_1 = 0.15\text{ m}$  and an outer radius  $R_2 = 0.76\text{ m}$ . The constant head tank had contractions, screens, and honeycombs that reduced turbulence. The bend and its upstream and downstream channels were made of plexiglas to facilitate the use of LDA and visual observations. To investigate the effects of vertical dividing concentric vanes on the bend flow characteristics, both 1-vane and 3-vane systems were used (Fig. 1 b,c). The vanes extended  $0.3\text{m}$  upstream and downstream of the bend. They were made of  $1.6\text{ mm}$  thick plexiglas plates, and the leading edges were bevelled (1:4). Details of flow conditions are presented in Table 1. The flow was subcritical and turbulent.

The velocity data were collected using a 2D Dantec LDA unit. The duration of each velocity measurement was 60 seconds with a sampling frequency varying between 20 Hz and 150 Hz depending on the flow zone. The error in velocity measurements is estimated to be 1%. 3D velocity measurements were obtained using two LDA probe orientations. In one probe orientation, the laser beam axis was parallel to the channel wall, and in another, it was parallel to the bed. This yielded the mean velocity components  $U$ ,  $V$  and  $W$  as well as the fluctuating velocity components  $u'$ ,  $v'$  and  $w'$  in the streamwise, lateral and vertical direction, respectively.

Because of the vane interference, 3D LDA measurements were restricted to the upstream and downstream cross-sections of the bend for the vane cases.

For the no-vane system, in the region G to H (Fig. 2), velocities were measured at 13 cross-sections (Fig. 2). At each cross-section, velocity measurements were taken at 21 lateral positions and 6 vertical positions corresponding to dimensionless heights  $z/Z$  equal to 0.07, 0.17, 0.28, 0.50, 0.72, and 0.89. At the two cross-sections further downstream (I,  $x_d = 3.0B$  and J,  $x_d = 4.0B$ ), velocity data were collected at 5 vertical ( $z/Z = 0.11, 0.33, 0.56, 0.78, \text{ and } 0.89$ ) and 13 lateral positions. For the configurations of bends with vanes, LDA measurements were taken at 5 cross-sections downstream of the bend (Fig. 1b,c). At each of these measuring cross-sections, 5 vertical ( $z/Z = 0.11, 0.33, 0.56, 0.78, \text{ and } 0.89$ ) and 13 lateral positions were sampled.

Following Sudo et al. (2001), the two following equations are used to calculate the intensity of secondary circulation  $I_s$  and the turbulence energy  $K_a$ , respectively:

$$I_s = \frac{1}{R_h^2 U_i^2} \int_0^Z \int_0^B (V^2 + W^2) dB dZ \quad (1)$$

$$K_a = \frac{1}{R_h^2 U_i^2} \int_0^Z \int_0^B \frac{1}{2} (\overline{u^2} + \overline{v^2} + \overline{w^2}) dB dZ \quad (2)$$

where  $R_h$  is hydraulic radius,  $U_i$  is the inlet velocity and the overbar indicates a time average.

To determine the dimensions of the flow separation zone, a cotton tuft of diameter 2mm was moved near the inner wall, to locate the flow separation point  $L_{u/s}$  and the reattachment point  $L_{d/s}$  (Fig. 1a) where the sign of  $U$  changes. This was followed by gently releasing a dye drop using a hypodermic needle. The dye used was a neutral buoyancy mixture of water-soluble

black ink and ethyl alcohol. A digital camera was used to record all observations. Using the dye test data, the length  $L_s$  (corresponding to the distance between  $L_{u/s}$  and  $L_{d/s}$ ) and the maximum width  $B_s$  of the separation zone adjoining the inner wall were obtained. The uncertainty in determining  $B_s$  and  $L_s$  in dye tests is estimated to be 10 mm. To confirm these estimated values of  $B_s$  and  $L_s$ , they were compared to streamwise velocity data from LDA measurements for the no-vane configuration. To this end, the values of  $U$  along a radial line were measured starting from the inner wall.  $U$  changes its sign from negative to positive further away from the wall. The value of  $B_s$  was approximated as the distance between the wall and the point where the net flow crossing the radial line is zero, whereas the length of the separation zone was determined by noting its end positions, where  $U$  changed signs near the inner wall. A comparison of values of  $B_s$  and  $L_s$  obtained from dye experiments and LDA computations at different heights above the bed for the no-vane case is presented in Table 2. The values are not statistically different (ANOVA p-values of 0.80 and 0.78 for  $B_s$  and  $L_s$ , respectively) and it was thus concluded that dye experiments could be used to determine separation zone dimensions for the vane configurations where no LDA measurements can be obtained in the bend section.

A standard 30° v-notch-tank system was used to measure the flow rate  $Q$ . The maximum error in the discharge measurement is estimated to be 3%. The inlet velocity was calculated based on  $Q$  and the measured flow depth  $Z$  upstream of the bed section (position F, Fig. 1a). To estimate the bend energy loss, the upstream specific energy ( $E_1$ ) at F and the downstream specific energy ( $E_2$ ) at I, located 1.81 m (= 3.0B) downstream of the bend exit (Fig. 1a) were computed as the water surface levels at F and I were nearly horizontal:

$$E = Z + \alpha \frac{U^2}{2g} \quad (3)$$

where the velocity distribution coefficient,  $\alpha$ , is:

$$\alpha = \frac{\sum_{i=1}^n U_a^3 A_i}{U^3 A},$$

where  $U_a$  is the average velocity for any segment of the cross section, and  $A_a$  is the area for that segment (Strum 2001). As the bed is horizontal, the specific energy loss ( $\Delta E = E_1 - E_2$ ) for the bend channel system also denotes the total energy loss.

Mean values of the free water surface levels were collected using a point gauge with an accuracy of 0.1 mm. During water surface profiling, significant fluctuations of the water surface level were noticed near the flow separation zone. Temporal fluctuations of the free water surface were recorded at a frequency of 16 Hz using three ultrasonic sensors, which sent out cone shaped sound pulses that were reflected by the water surface (Lundhal DCU 7110). The data logger (Campbell CR5000) recorded the time intervals between the transmitted and received signals, and converted them into a distance between the water surface and the sensor (ITRC 1998).

## Results

### ***No-vane system***

The three velocity components  $U$ ,  $V$ , and  $W$  were used to compute the mean velocity vector  $U_T = \sqrt{(U^2 + V^2 + W^2)}$ . For the flow condition described in Table 1, Fig. 3 shows the contour plots of  $U_T$  with superimposed vector plots of  $V$  and  $W$  at three heights above the bed. In all cases, flow accelerates near the inner wall and decelerates near the outer wall of the bend ( $\theta = 45^\circ$ ) due to the favourable and unfavourable streamwise pressure gradients. As the flow enters the bend, the strength of the secondary flow increases. Planform vectors are generally oriented

towards the inner wall near the channel bed (Fig. 3a) and towards the outer wall near the water surface (Fig. 3c). Secondary flow becomes more intense as the flow reaches the bend exit, and the fast flow near the inner wall is convected towards the outer wall by the secondary flow.

As the flow crosses the central section of the bend ( $45^\circ < \theta < 50^\circ$ ), the lateral slope of the water surface starts to recover (Fig. 4), and the flow begins to accelerate near the outer wall and to decelerate near the inner wall, leading to the separation of flow at the inner wall (Fig. 3). The upstream location of the flow separation zone  $L_{u/s}$  is close to  $\theta \approx 50^\circ$  for all heights above the bed (Fig. 3), which also corresponds to the onset of the adverse pressure gradient along the inner wall (Fig. 4). However, the reattachment point  $L_{d/s}$  is located further downstream near the water surface, indicating that  $L_s$  reaches its maximum value near the free surface (Fig. 3c). The values of  $L_s$  and  $B_s$  recorded near the free surface are respectively 55 cm and 9 cm, whereas the values of  $L_s$  and  $B_s$  recorded near the bed are respectively 32 cm and 2 cm (Table 2).

The water surface difference between the super-elevation zone at the outer radius and the water surface depression at the inner radius is 0.75 cm (Fig. 4). This corresponds to 8.8% of the average flow depth. The maximum water surface elevation is in the bend region along the outer wall ( $45^\circ < \theta < 50^\circ$ ), and the minimum water surface elevation is near the  $50^\circ$  cross-section along the inner wall. The lateral slope of water surface disappears over a short distance ( $x_d/B = 1.2$ ) in the downstream channel.

Near the reattachment point at the inner wall, the flow was observed to be slightly unsteady near the free surface, due to the vertical current moving towards the water surface at the inner wall. Time series of the water surface fluctuations recorded by acoustic sensors reveal larger root mean square (rms) values along the inner wall (rms = 2.5 mm) than along the outer

wall (rms = 1.8 mm), confirming that water surface fluctuations are more intense along the inner wall near the flow separation zone than along the outer wall (Fig. 5).

The development of secondary flow circulation in the bend is more clearly identified from the lateral and vertical velocity vector plots (Fig. 6). There is an upward movement of the flow close to the inner radius and a downward movement near the outer radius associated with a clockwise secondary flow cell (Fig. 6a-f). A weaker counter-rotating secondary flow cell near the free surface of the outer wall is also present. The presence of such a weaker counter-rotating secondary flow cell has been observed in previous studies of flow in bends (Blanckaert and Graf 2001; Booij 2003). These two secondary flow cells gain strength as they move further downstream of the bend (Fig. 6b-d), as illustrated by the increase in the magnitude of the lateral velocity. Later, these cells weaken as they move into the straight downstream channel (Fig. 6f,g). For the present flow configuration of the bend with no vanes ( $B/Z = 6.8$ ),  $V$  is expected to be much larger than  $W$ . Hence, for the secondary flow generated in the downstream channel,  $V$  is the dominant component contributing to the intensity of secondary flow  $I_s$  (Eq 1). As such, large reduction of  $V$  will manifest as a drastic reduction of  $I_s$ .

Only limited experimental studies related to the measurement of turbulence quantities for flow around bends exist (Booij 2003; Blanckaert 2009; and Sanjou and Nezu 2009). The total turbulent kinetic energy ( $ke$ ) is calculated using the variance of the turbulent velocity measurements as:

$$ke = \frac{1}{2}(\overline{u^2} + \overline{v^2} + \overline{w^2}) \quad (4)$$

An area of high  $ke$  exists between the separation zone and the high velocity zone (Fig. 7). This can be related to the shear zone between the accelerated fast moving flow just outside the separation bubble and the very slow moving flow in the recirculation zone. In the downstream

part of the bend ( $50^\circ < \theta < 90^\circ$ ),  $ke$  weakens. For the region close to the free surface where flow separation is the largest, Fig. 8 shows the contour plots of rms values of the lateral ( $v_{rms}$ ) and vertical ( $w_{rms}$ ) turbulent velocity components normalized by the streamwise turbulent velocity component ( $u_{rms}$ ). A marked variation of  $v_{rms}/u_{rms}$  (Fig. 8a) is apparent in the counter rotating secondary flow cell zone near the top of the outer wall. Furthermore, a significant variation of the ratio  $w_{rms}/u_{rms}$  (Fig. 8b) is apparent in the flow separation zone near the inner wall. This suggests that the isotropic assumption used in most computational fluid dynamics (CFD) turbulence models might result in significant errors when predicting the flow field around an open channel bend.

### **Bends with Vanes**

The mean velocity fields for the 1-vane and the 3-vane systems are presented in Fig. 9. For these vane systems, the distribution of streamwise velocity  $U$  is more uniform than in the no-vane case. For the 3-vane system, flow is even more uniform than for the 1-vane system. Lateral and vertical velocity plots reveal the presence of two and four secondary flow cells for the 1-vane and the 3-vane systems, respectively at  $x_d/B = 1$  and 2 (Fig. 10). Compared to the no vane system (Fig. 6c-g), the secondary flow pattern is markedly different and much weaker, especially in the 3-vane system (Fig. 10). For the no-vane system, a large shift of accelerated high velocity flow from the inner wall towards the outer wall was observed (Fig. 3). However, a less significant shift of flow is noticed for the 1-vane system (Fig. 9a,b), and an even less important shift is observed for the 3-vane system (Fig. 9c,d). The contour plots of  $U_T$  and vectors indicate that flow recovers rapidly to form a nearly uniform flow at  $x_d/B = 4.0$ , in particular for 3-vane system (Fig. 10b).

The dimensions of the separation zone are also markedly reduced in the presence of vanes (Table 2). A reduced flow separation zone is noticed only near the inner wall of the bend with vanes, and no flow separation is discerned in the vicinity of the vanes. Compared to the no-vane system, for the 3-vane system, the length and width reductions of the zone of flow separation are 65% and 62%, respectively.

The magnitude of  $ke$  is also noticeably reduced for bends with vanes (Fig. 11). Besides the high turbulence zone near the inner wall due to the flow separation, local pockets of high turbulence are observed downstream of each vane for both vane configurations (Fig. 11). Highly sheared flows occur just downstream of the vane tips, since all the merging pairs of secondary flow cells rotate clockwise (looking downstream, Fig. 10). These result in local high turbulence zones marked as  $l$ ,  $m$ ,  $n$ , and  $o$  in Fig. 11, at the cross-section immediately downstream of the vanes. The local high turbulence zone near the inner wall persists further downstream from the bend, but the turbulence pockets associated with the vanes decay rapidly, mainly for the 3-vane system (Fig. 11b).

The variations of parameters  $I_s$  and  $K_a$  along the channel downstream of the bend are shown in Fig. 12. Compared to the no-vane system, for the 1-vane system, the value of  $I_s$  ( $= 0.6$ ) is smaller at the exit of the bend. For the 3-vane system,  $I_s$  at the end of the bend ( $= 0.18$ ) is still smaller compared to the 1-vane system. In the 3-vane system,  $I_s$  reaches the lowest asymptotic value ( $I_s = 0.003$ ) over a very short distance at  $x_d/B = 4.0$  downstream of the bend (Fig. 12a). In all 3 systems, there is a very large and rapid decay of  $I_s$  from the exit of the bend to a downstream location where  $x_d/B = 2.0$ . The rate of decay becomes further reduced downstream in the straight channel (Fig. 12a). Blanckaert (2009) and Zeng et al. (2008) used circulation strength of the normalized depth-averaged cross-stream to indicate the development of the

secondary flow in a  $193^\circ$  open-channel bend. Their studies showed that the secondary circulation and turbulent kinetic energy intensified as the flow passed the bend section, and peaked at the cross-section at  $90^\circ$ . This strong secondary flow diminished further downstream of the bend, and the reported distance for the strength of secondary flow to reach its asymptotic value in the downstream channel was close to our observations of  $2.0B$ .

The initial value of  $K_a$  at the exit of the bend is relatively high for the no-vane system. It is lower for the systems with vanes (Fig. 12b). For all three systems,  $K_a$  generally decays rapidly as the flow leaves the bend and enters the downstream channel. In the 3-vane system,  $K_a$  reaches the lowest asymptotic value ( $K_a = 0.04$ ) in a very short distance at  $x_d/B = 4.0$  downstream of the bend (Fig. 12b). For the no vane system, the residual turbulence is relatively high ( $K_a=0.089$ ) at  $x_d/B = 4.0$ , and has not reached the asymptotic value of  $K_a = 0.04$ . One notices a slight increase of  $K_a$  for the 3-vane system between the bend exit and  $x_d/B = 1.0$ . This may be directly traced to the local shear generated by the adjacent merging pairs of secondary flow cells that emerge from the subareas of the 3-vane system. As stated earlier, these secondary flow cells are rotating in the same direction, and hence generate a highly sheared flow when they meet at the tip of the vanes. Values of both  $I_s$  (insert, Fig. 12a) and  $K_a$  (Fig. 12b) are the lowest for the 3-vane system, indicating that this bend-vane configuration is very effective in reducing intensities of both secondary flow and turbulence.

The specific energy loss  $\Delta E$  between locations F and I (Fig. 1a), which also denotes the total energy loss, is  $0.16$  cm for the no-vane system (Fig. 4). For both bend systems with vanes,  $\Delta E$  is  $0.13$ cm. Hence, the energy loss is smaller for the systems with vanes. Although the 3-vane system provides a more uniform flow compared to the 1-vane system, possibly the increased boundary friction losses in the former results in similar energy loss for both systems. As such, in

practice, only fewer vanes need be used in the case with vanes, if energy conservation is a primary goal.

## Summary and Conclusion

The study reveals marked differences in the mean and turbulent flow characteristics for flows in bends with and without vanes. The three-dimensional flow characteristics in a rectangular open-channel 90° bend (no-vane system) compare well with the large number of studies that have highlighted the existence of multiple secondary flow cell structures in open-channel bends. The results confirm the existence of a main inner bank cell and a counter-rotating, weaker outer bank cell in the channel downstream of the bend.

The adverse pressure gradient caused by the rapid recovery of the water surface along the inner wall ( $\theta = 50^\circ$ ) induces a large flow separation zone for the bend with no vanes. For bends with vanes, the extent of flow separation zone is drastically reduced along the inner wall, especially for the 3-vane system. Higher degree of flow separation leads to increased energy losses caused by higher turbulence. An anisotropic high turbulence zones exist near the flow separation zone and persists for long distances downstream, especially for the no vane system. Consequently, only advanced turbulence models that can properly resolve all Reynolds stress components can adequately simulate sharp bend flows.

At the exit of the bend, the intensity of secondary flow  $I_s$  and turbulence energy  $K_a$  are much smaller for flow in a bend with vanes compared to the bend with no vanes. For the former, the low asymptotic values of  $I_s$  ( $= 0.003$ ) and  $K_a$  ( $= 0.005$ ) are quickly reached at  $x_d/B=4.0$  in the downstream channel. However, for the no-vane system, the residual values of  $I_s$  ( $= 0.007$ ) and  $K_a$  ( $= 0.089$ ) are still high at  $x_d/B = 4$  and they still have not reached their asymptotic values. The

improved performance in bend flows when vanes are present can be attributed to the reduced ratio of width to depth in the subsections of the bend. This results in a drastic reduction of the intensity of secondary flow ( $I_s$ , Fig. 12a). More uniform flow is established both in the bend and in the downstream channel due to the presence of vanes. For instance, the maximum value of  $U$  near the inner wall at  $\theta = 45^\circ$  is 50% more for the bend with no-vane compared to the maximum value of  $U$  for the bend with 3-vanes. Bends with vanes have lower intensity of secondary flow besides having a lower value for the maximum value of  $U$ . These features contribute to a decrease in the tendency for channel erosion in unlined channels. Further, results indicate that vanes are effective in slightly reducing energy losses which in turn permits an increase in the area subject to irrigation. Sharp bends have been discouraged in practice to avoid excessive secondary flows and severe flow separation, but the present results show that using vanes can help mitigate the negative impacts of sharp bends. Furthermore, the more uniform water surface in bends with vanes can reduce free board demand, thus decreasing construction cost.

The recommendations that the findings of this study suggest are that vanes could be added in future designs of irrigation channels with sharp bends. They are useful to reduce the separation zone along the inner wall and generate a more uniform flow. The findings that vanes reduce flow separation, secondary flows and energy loss in sharp bends were also confirmed by a 3D model, which allows the flow field to be predicted in zones not accessible with the LDA between vanes (Han et al., in review).

In the case of bends with vanes, differential hydrodynamic forces are present due to the large pressure differences on either side of the curved vane surfaces. As such, they have to be well anchored below the bed. Further, simple spacers at the top the vanes at a few sections will allow the vane system to be more robust and stable. For a field version of these experimental

vanes, it may be appropriate to use thin continuous stainless steel plates having 9 segments ( $10^\circ$ ) rather than a single curved ( $90^\circ$ ) vane. However, the feasibility of this arrangement should be verified by laboratory experiments or numerical simulations. Considering the difficulties of obtaining 3D velocity data close to vanes in experimental studies, a 3D numerical model similar to that used by Han et al. (in review) would be required to pursue these investigations.

### **Acknowledgements**

The comments of two anonymous reviewers on a previous version of this paper have helped improving it.

## Nomenclature

*The following symbols are used in this paper:*

$A_i$  = area for any segment of the cross section ( $m^2$ );

$B$  = flume width (m);

$B_s$  = maximum width of separation zone (cm);

$I_s$  = intensity of secondary flow;

$K_a$  = turbulence energy;

$ke$  = total turbulence kinetic energy ( $m^2/s^2$ );

$L_s$  = length of flow separation zone (cm);

$L_{w/s}$  = start location of flow separation zone;

$L_{d/s}$  = reattachment location of flow separation zone;

$Q$  = flow rate ( $m^3/s$ );

rms = root mean square;

$R$  = mean radius of the bend (m);

$R_1$  = inner radius (m);

$R_2$  = outer radius (m);

$R_h$  = hydraulic radius (m);

$U$  = streamwise velocity (m/s);

$U_a$  = average velocity for sub segment of the cross section (m/s);

$U_i$  = average velocity for sub segment of the cross section (m/s);

$U_T$  = mean velocity vector (m/s);

$u'$ ,  $v'$ , and  $w'$  = fluctuating velocities in streamwise, lateral, and vertical directions in the measuring volume, respectively (m/s);

$u_{rms}$ ,  $v_{rms}$ , and  $w_{rms}$  = root mean square values of streamwise, lateral, and vertical turbulent velocity components (m/s);

$V$  = lateral velocity (m/s);

$W$  = vertical velocity (m/s);

$x_d$  = downstream distance from 90° of bend (m)

$x_u$  = upstream distance from 90° of bend (m)

$z$  = elevation above bed (m).

$Z$  = flow depth (m);

## References

- Abad, J. D., Rhoads, B. L., Guneralp, I., García, M. H. (2008). "Flow structure at different stages in a meander-bend with bendway weirs." *J. Hydraulic Engineering*, ASCE, 138(8), 1052-1063.
- Barlow, J. B., Rae, W. H., Jr., and Pope, A. (1999). "Low-Speed Wind Tunnel Testing", 3rd Edition, New York: John Wiley & Sons, Inc.
- Blanckaert, K. and Graf, W. H. (2001). "Mean flow and turbulence in open-channel bend." *J. Hydraulic Engineering*, ASCE, **127**(10), 835-847.
- Blanckaert, K. and de Vriend, H. J. (2004). "Secondary flow in sharp open-channel bends." *J. Fluid Mechanics*, Cambr. Univ. Press, **498**, 353-380.
- Blanckaert, K., and Lemmin, U. (2006). "Means of noise reduction in acoustic turbulence measurements." *J. Hydraulic Research*, IAHR, **44**(1), 3 – 17.
- Blanckaert, K. (2009). "Saturation of curvature-induced secondary flow, energy losses, and turbulence in sharp open-channel bends: Laboratory experiments, analysis, and modeling." *J. Geophysical Research*, 114.
- Booij, R. (2003). "Measurements and large eddy simulations of the flows in some curved flumes". *J. Turbulence*, **4**, 1–17.
- Derrick, D. L. (1997). "Harland creek bendway weir/willow post bank stabilization demonstration project." Management of landscapes disturbed by channel incision, S. S. Y. Wang, E. J. Langendoen, and F. D. Shields, Jr., eds., University of Mississippi Press, Oxford, Miss., 351–356.
- Dietrich, W. E. and Smith, J. D. (1983). "Influence of the point bar on flow through curved Channels." *Water Resources Research*, 19(5), 1173-1192.
- De Vriend, H. J. (1977). "A Mathematical Model of Steady Flow in Curve Shallow Channels." *J. Hydraulic Research*, **15**(1), 37-53.
- De Vriend, H. J. (1981). "Velocity redistribution in curved rectangle channels." *J. Fluid Mechanics*, **107**(6), 423-439.
- Han, S.S., Biron, P.M. and Ramamurthy, A.S (in review). "Three-dimensional modeling of flow in open-channel sharp bends with vanes." *J. Hydraulic Research*.
- Hyun, B. S., Balachandar, R., Yu, K. and Patel, V. C. (2003). "Assessment of PIV to measure mean velocity and turbulence in open-channel flow." *Experiments in Fluids*, **35**(3), 262-267.

- Ippen, A. and Drinker, P. A. (1962). "Boundary shear stresses in curved trapezoidal channels." *J. Hydraulics Division, ASCE*, 143-179.
- Ishigaki, T., Shiono, K., and Rameshwaran, P. (2002). "PIV and LDA Measurements of Secondary flow in a meandering channel for overbank flow." *J. Visualization*, **5**(2), 153-159.
- ITRC (Irrigation Training and Research Center) (1998). "Water level sensor and data logger testing and demonstration." Cal Poly.
- Jia, Y., Scott, S. H., Xu, Y., Huang, S., and Wang, S.S.Y, (2005). "Three-dimensional numerical simulation and analysis of flows around a submerged weir in a channel bendway." *J. Hydraulic Engineering*, 131 (8), 682-693.
- Kalkwijk, J. P. and de Vriend, H. J. (1980). "Computation of the flow in shallow river bends." *J. Hydraulic Research, IAHR*, **18**(4), 327-341.
- Luo, J. and Razinsky, E.H. (2009). "Analysis of turbulent flow in 180 deg turning ducts with and without guide vanes." *J. Turbomachinery, ASME*, **131**(2), 021011
- Odgaard, A.J. and Kennedy, J. F. (1983). "River-bend bank protection by submerged vanes." *J. Hydraulic Engineering*, **109**(8), 1161-1173.
- Odgaard, A. J. and Spoljarec, A. (1986). "Sediment Control by Submerged Vanes." *J. Hydraulic Engineering, ASCE*, **112**(12), 1164–1181.
- Odgaard, A. J. and Spoljarec, A. (1989). "Sediment Control by Submerged Vanes." In: Ikeda, S. and Parker, G.(eds), Design Basis. River Meandering, Water Resources Monograph No. 12, American Geophysical Union, 127–151.
- Odgaard, A. (1989a). "River meander model. I: Development." *J. Hydraulic Engineering*, **115**(11), 1433–1450.
- Odgaard, A. (1989b). "River meander model. II: Application." *J. Hydraulic Engineering, ASCE*, **115**(11), 1451–1464.
- Odgaard, A. J., and Wang, Y. (1991a). "Sediment management with submerged vanes. I: Theory." *J. Hydraulic Engineering, ASCE*, **117**(3), 267-283.
- Odgaard, A. J., and Wang, Y. (1991b). "Sediment management with submerged vanes. II: Applications." *J. Hydraulic Engineering, ASCE*, **117**(3), 284-302.
- Przedwojski, B., Blazejewski, R., and Pilarczyk, K. W. (1995). "River Training Techniques: Fundamentals, Techniques and Applications." *Balkema, Rotterdam, The Netherlands*.

- Reinauer, R. and Hager, W. H. (1997). "Supercritical bend flow." *J. Hydraulic Engineering*, ASCE, **123**(3), 208-218.
- Roca, M., Martín Vide, J. P., and Blanckaert, K. (2007). "Reduction of bend scour by an outer bank footing: Footing design and bed topography." *J. Hydraulic Engineering*, ASCE, **133**(2), 139-147.
- Roca, M., Blanckaert, K., and Martín-Vide, J. P. (2009). "Reduction of bend scour by an outer bank footing: Flow field and turbulence." *J. Hydraulic Engineering*, ASCE, **135** (5), 361-368.
- Rozovskii, I. L. (1957). "Flow and water in bends open channels." Academy of Sciences of the Ukrainian SSR, *Isr. Progr. Sc. Transl.*, Jerusalem, Israel.
- Sahlin, A. and Johansson, A. V. (1991). "Design of guide vanes for minimizing the pressure loss in sharp bends." *Physics of Fluids A3*, 1934-1940.
- Sanjou, M and Nezu, I. (2009). "Turbulence structure and coherent motion in meandering compound open-channel flows", *J. Hydraulic Research*, **47**(5), 598-610.
- Shukry, A. (1949). "Flow around bends in an open flume." *Transactions*, ASCE, **115**, 751-788.
- Strum, T. (2001). "Open Channel Hydraulics." McGraw-Hill, New York.
- Sudo, K., Sumida, M., and Hibara, H. (2001). "Experimental investigation on turbulent flow in a square-sectioned 90° bend", *Experiments in Fluids*, **30**, 246-52.
- Thornton, C. I., Heintz, M. L., Abt, S. R., Baird, D. C. and Padilla, R. S. (2005) "Effects of bendway weir characteristics on resulting flow conditions." ASCE conference Proceedings 173, 578, DOI:10.1061/40792(173)578
- Tominaga, A., Nagao, M., and Nezu, I. (1999). "Flow structure and momentum transport processes in curved open-channels with vegetation." Proc., 28th Congr. Int. Assoc. Hydr. Res., Technical University of Graz, Austria (CD-ROM)
- Tominaga, A. and Nagao, M. (2000). "Secondary flow structure in bends of narrow open channels with various cross sections." 4<sup>th</sup> international conference on hydro-science and engineering, 2(1) (CD-ROM)
- US Army Corps of Engineers, 1994. "Hydraulic Design of Flood Control Channels.", US Army Corps of Engineers Engineer Manual EM 1110-2-1601.
- Wetzel, J. and Arndt, R.E.A. (1994). "Hydro dynamic design considerations for hydroacoustic facilities: I flow quality.", *J. Fluid Engineering*, **116**(2), 324-331.
- Zeng, J., Constantinescu, G., and Weber, L. (2008). "A 3D non-hydrostatic model to predict flow and sediment transport in loose-bed channel bends." *J. Hydraulic Research*, **46** (3), 356-372.

**Table 1.** Experimental Flow conditions

Channel width (B)	Flow depth (Z)	Inner radius (R1)	Outer radius (R2)	Flow rate (Q)	Inlet mean velocity (U)	Reynolds number (Re)	Froude number (Fr)
0.61m	0.091m	0.15m	0.76m	0.013m <sup>3</sup> /s	0.238m/s	15870	0.252

Note:  $U=Q/BZ$ ;  $Fr=U/\sqrt{gZ}$ ; and  $Re=UZ/\nu$ , where  $\nu$  is kinematic viscosity.

**Table 2.** Dimensions of inner wall flow separation zone for the no-vane, 1-vane, and 3-vane systems.

Location above bed z (cm)	Length ( $L_s$ , cm)			Width ( $B_s$ , cm)		
	No vane	1 Vane	3 Vanes	No vane	1 Vane	3 Vanes
2.0	32 (30)	13	0	2 (1.5)	1	0
4.0	40 (35)	21	5	5 (4.4)	3	1
6.0	51 (51)	24	15	7 (6.5)	6	2
8.0	55 (54)	28	18	9 (8.2)	5	3

Note: values in brackets are from calculation using LDA velocity measurements.

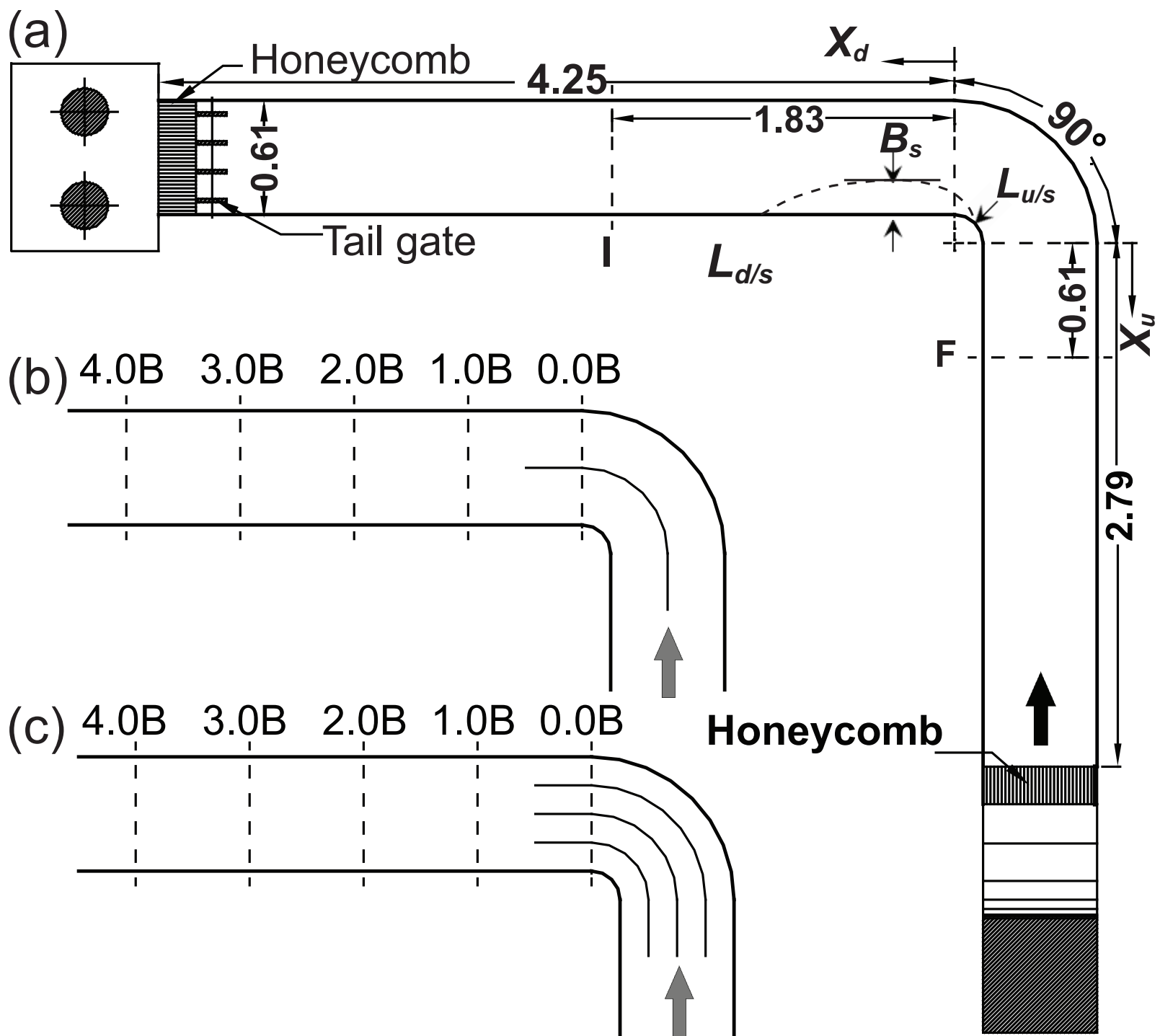


**Fig. 1.** (a) Layout of the flume (dimensions are in meters); zoomed bend and downstream sections with the position of the measured cross sections (distances based on the width ( $B=0.61$  m)) for the configurations using (b) 1 vane; (c) 3 vanes.

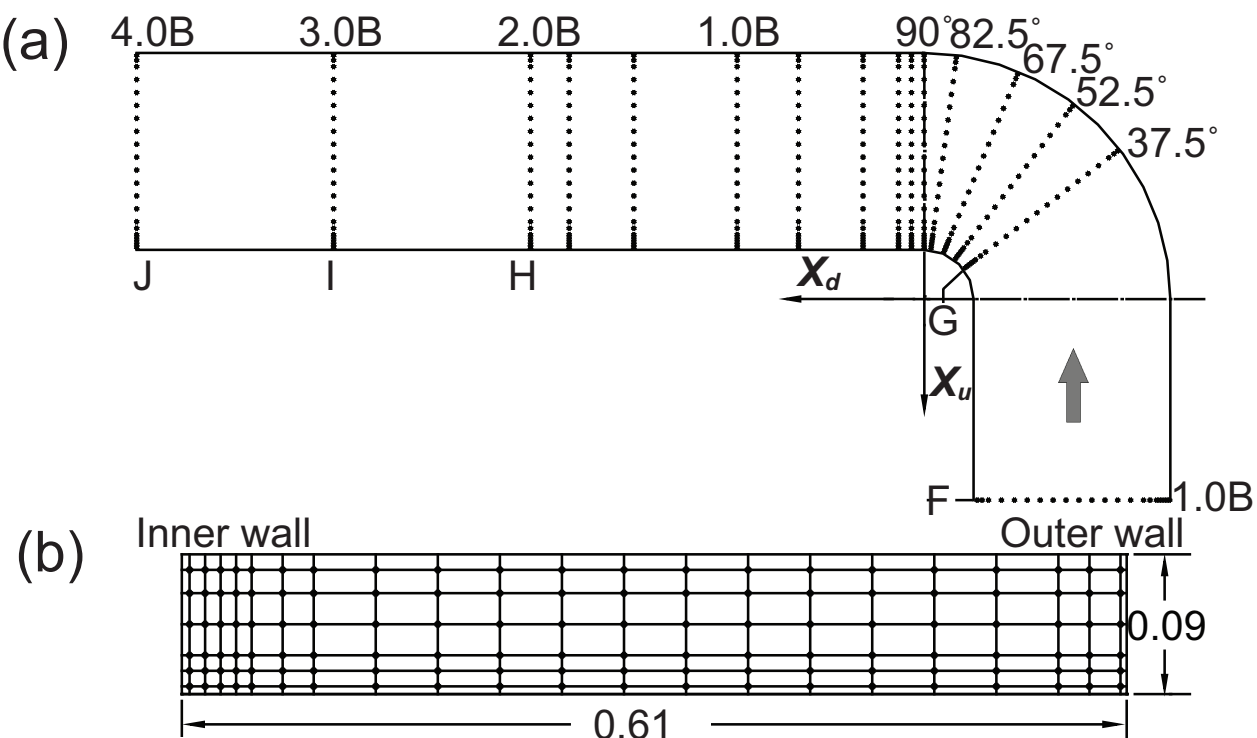


**Fig. 2.** (a) Planform positions for LDA velocity measurements; (b) measuring points for no-vane system.

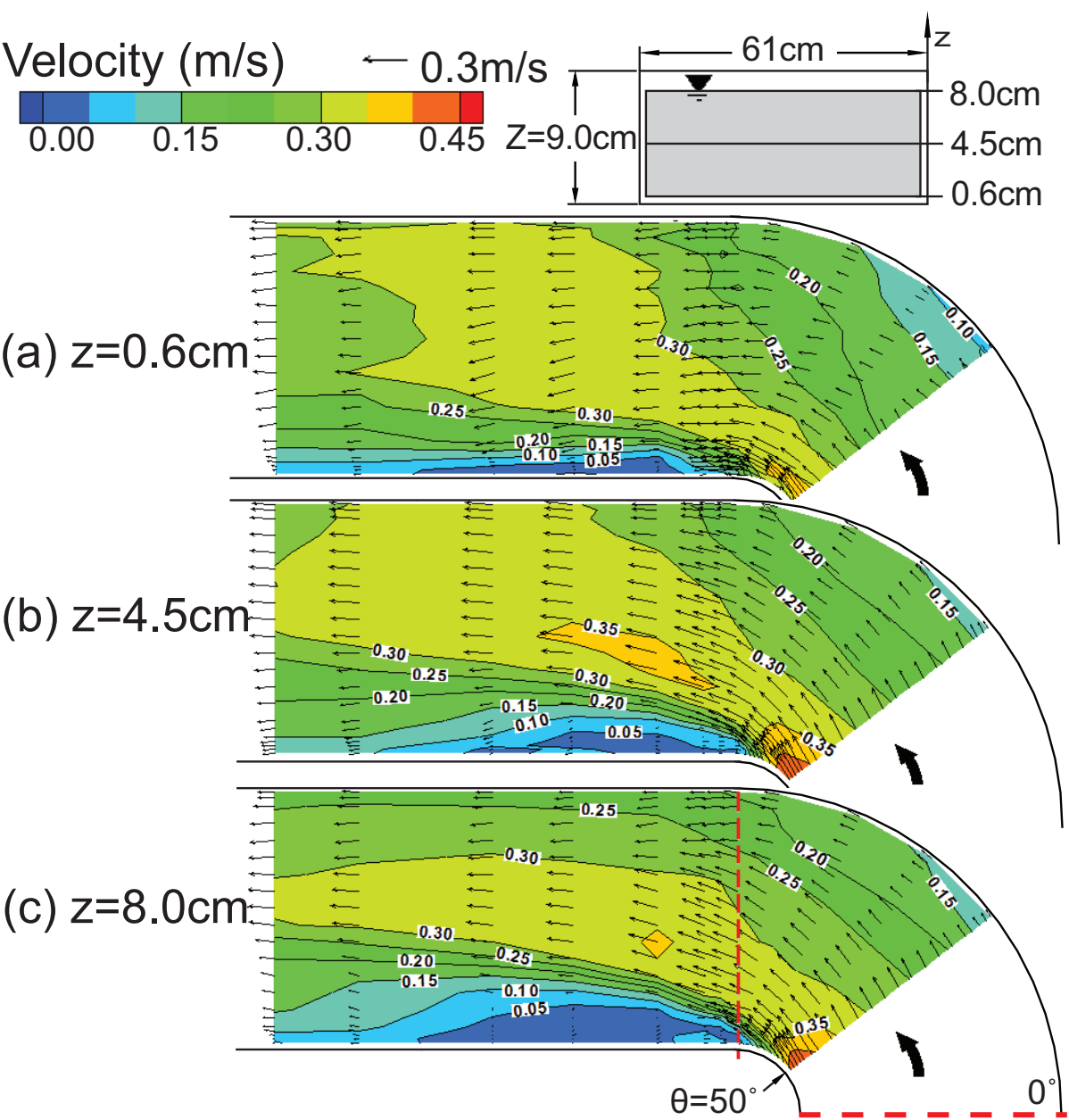


**Fig. 3.**  $U$ - $V$  vectors overlaid on contour plots of  $U_T$

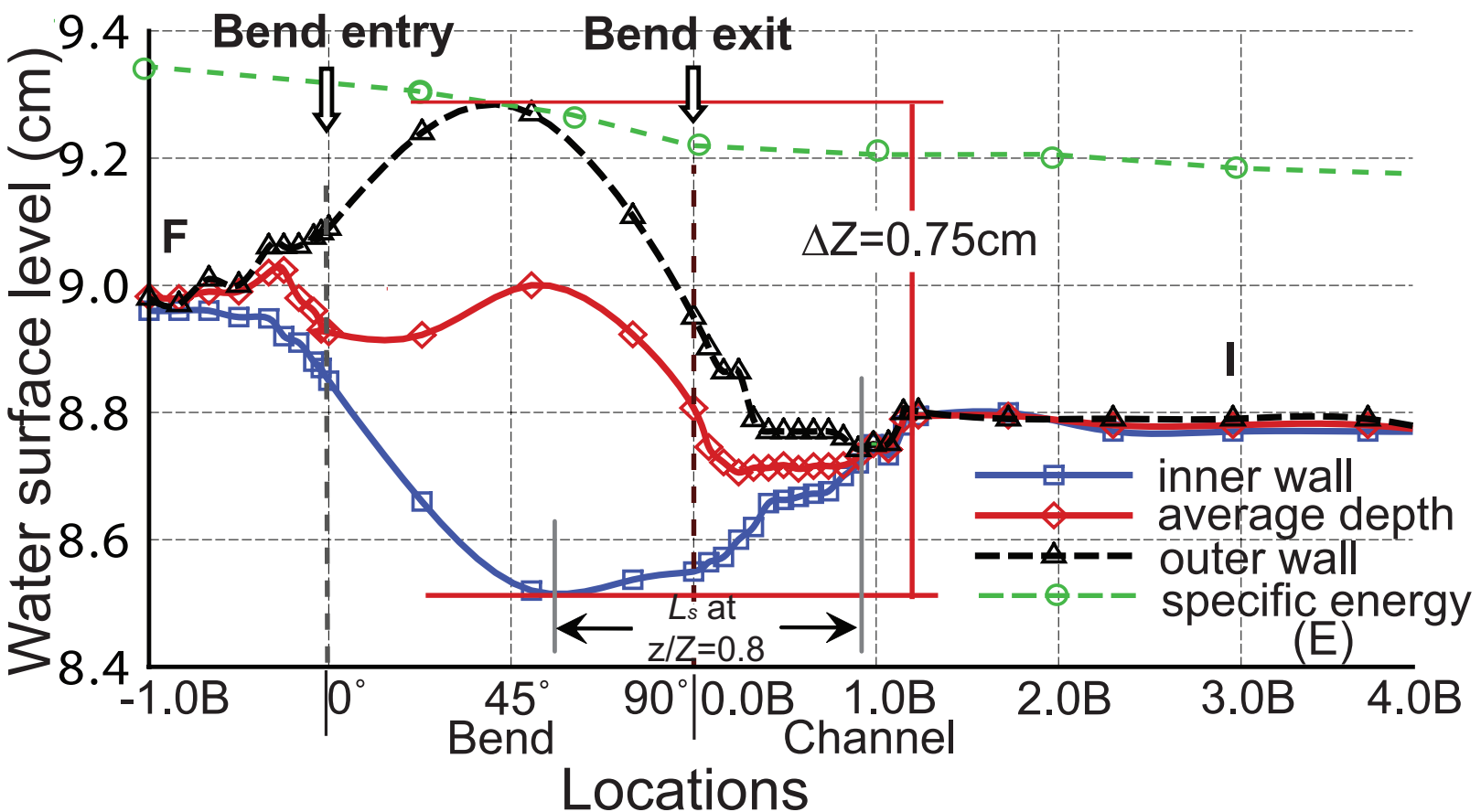


**Fig. 4.** Water surface profiles at inner (blue squares) and outer (black triangles) walls with average water depth (red diamonds) and specific energy (green circles). Bend locations are in terms of  $\theta$  and channel locations are in terms of  $B$

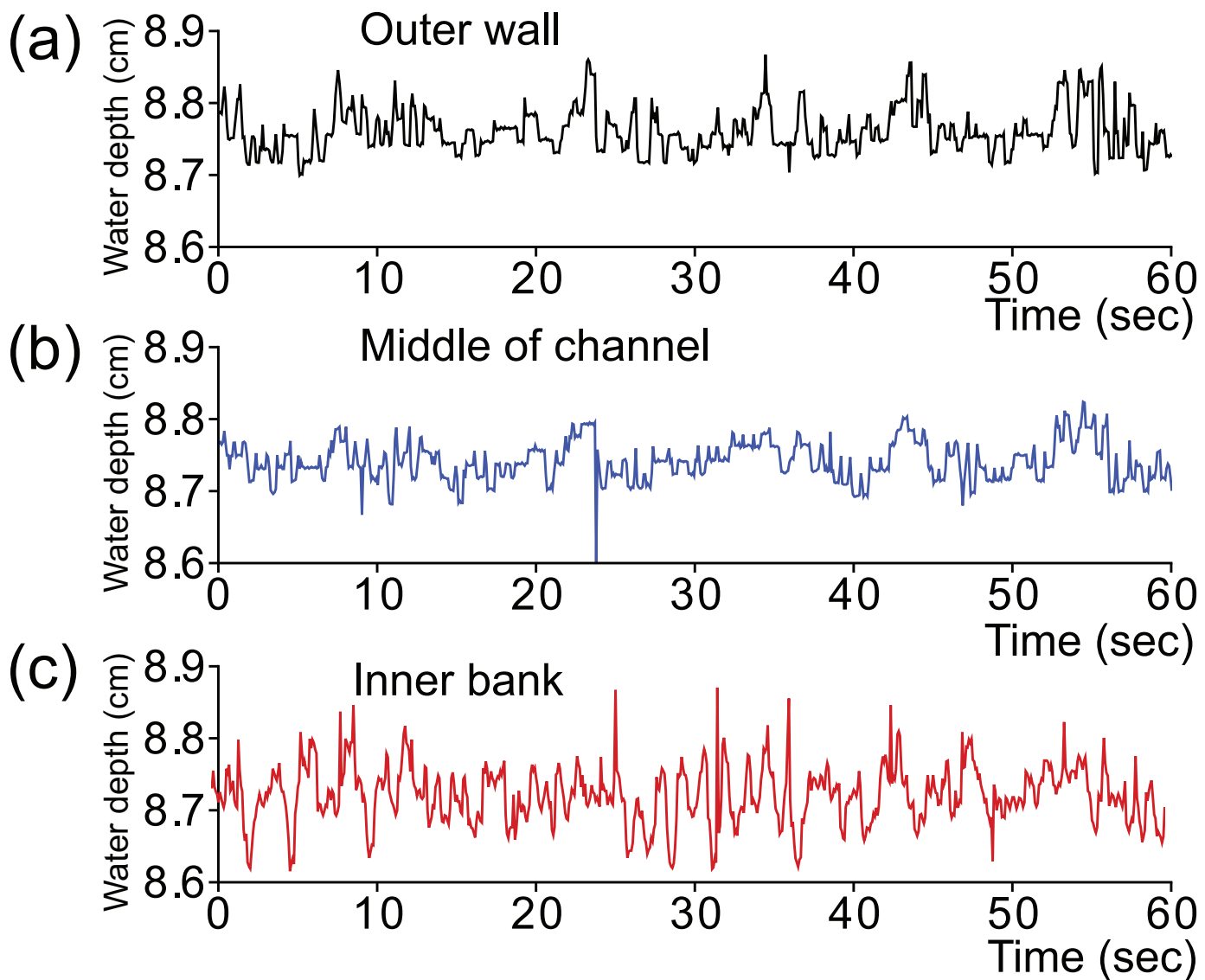


**Fig. 5.** Measured water surface level fluctuations at 0.1 B downstream of the bend: (a) outer wall; (b) middle of channel; (c) inner wall

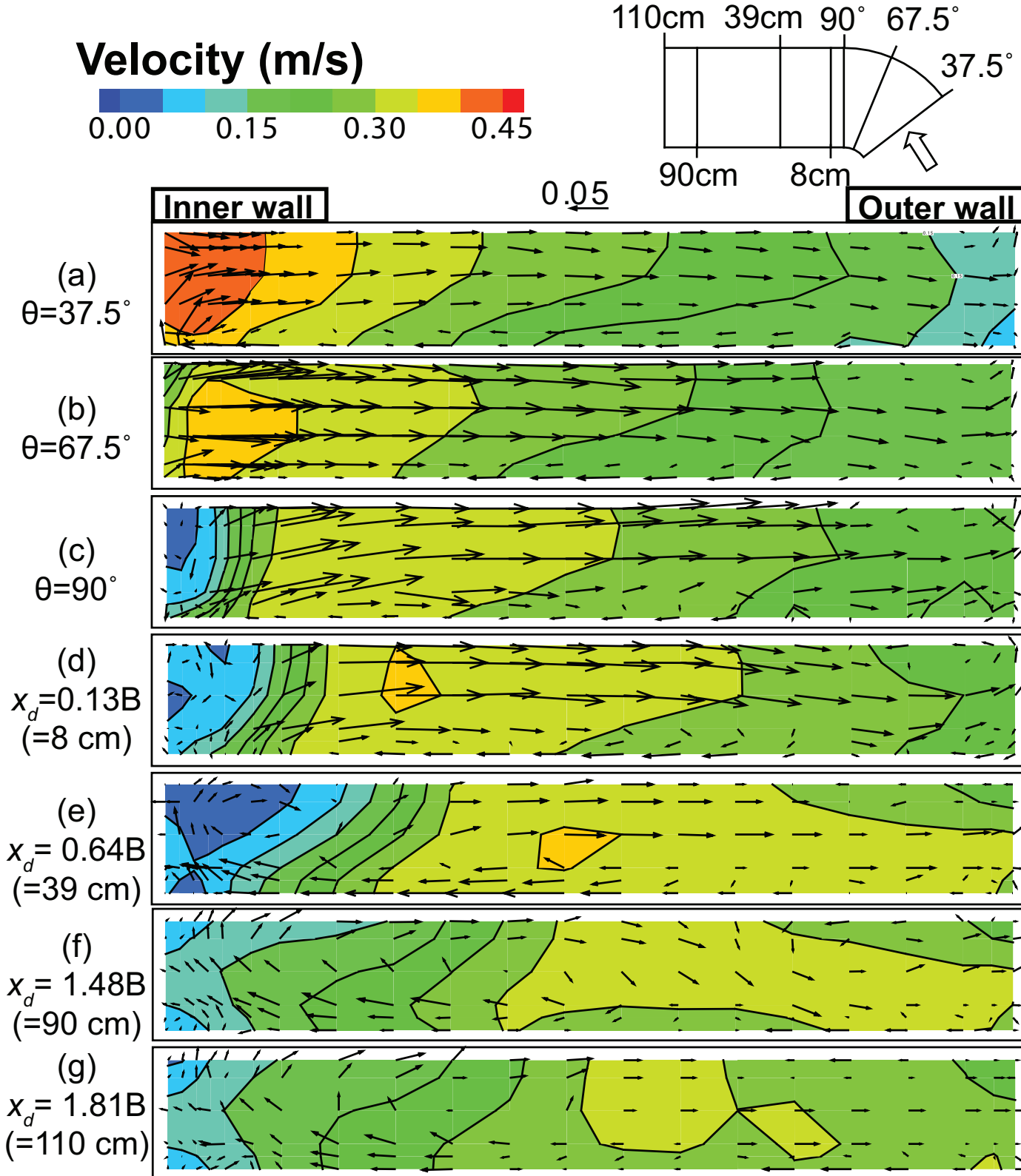


**Fig. 6.** Vector plots of lateral and vertical velocity superimposed on contours of velocity magnitude (looking downstream) in the bend cross-sections at positions: (a)  $37.5^\circ$ ; (b)  $67.5^\circ$ ; (c)  $90^\circ$ ; and in the downstream channel at cross-sections (d)  $0.13B$  (=8 cm); (e)  $0.64B$  (=39 cm); (f)  $1.48B$  (=90 cm) and (g)  $1.81B$  (=110 cm).

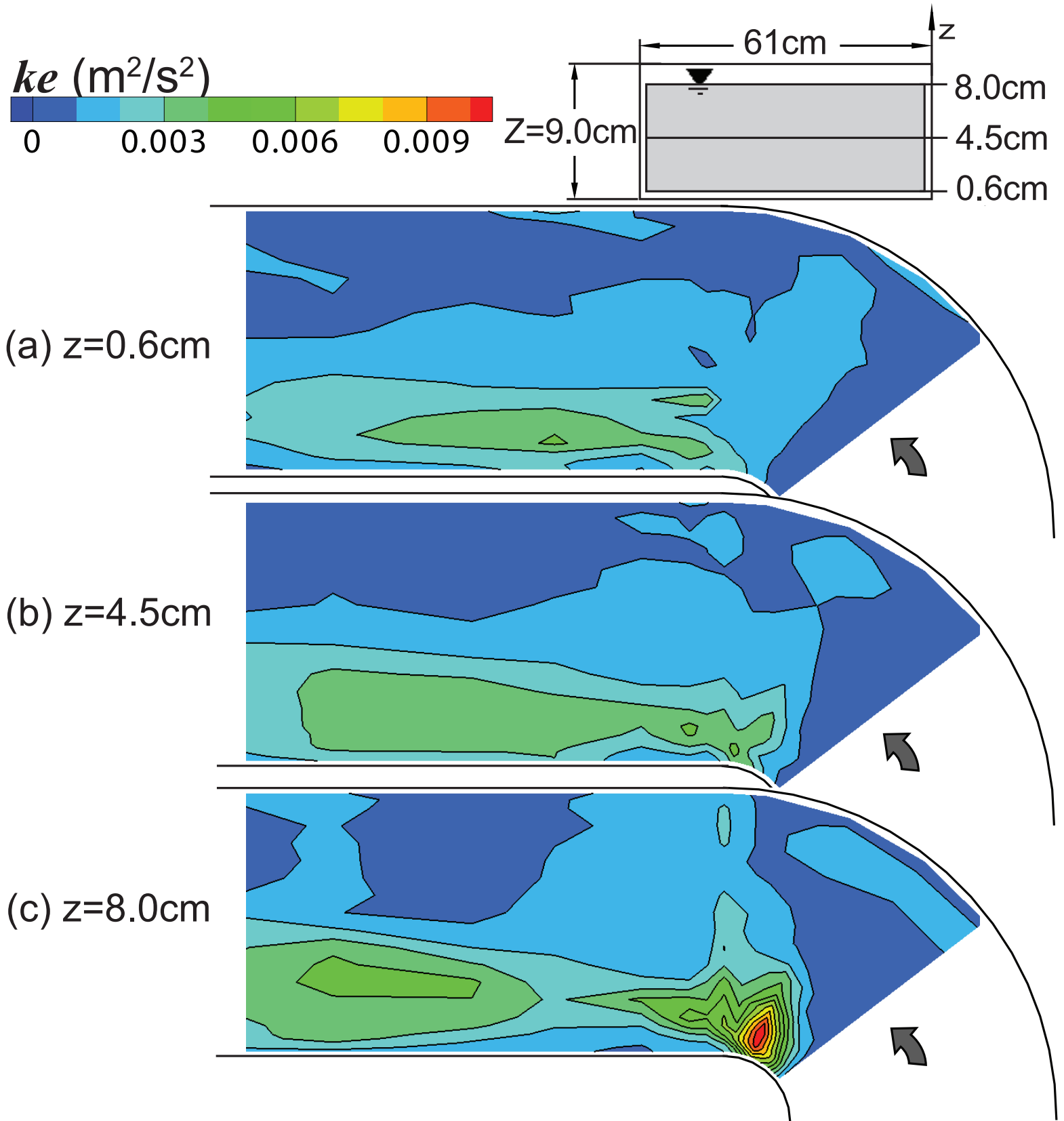


**Fig. 7.** Contour plots of turbulent kinetic energy ( $ke$ ) at dimensional heights above bed ( $z/Z$ ) of a) 0.07, b) 0.50 and c) 0.88.

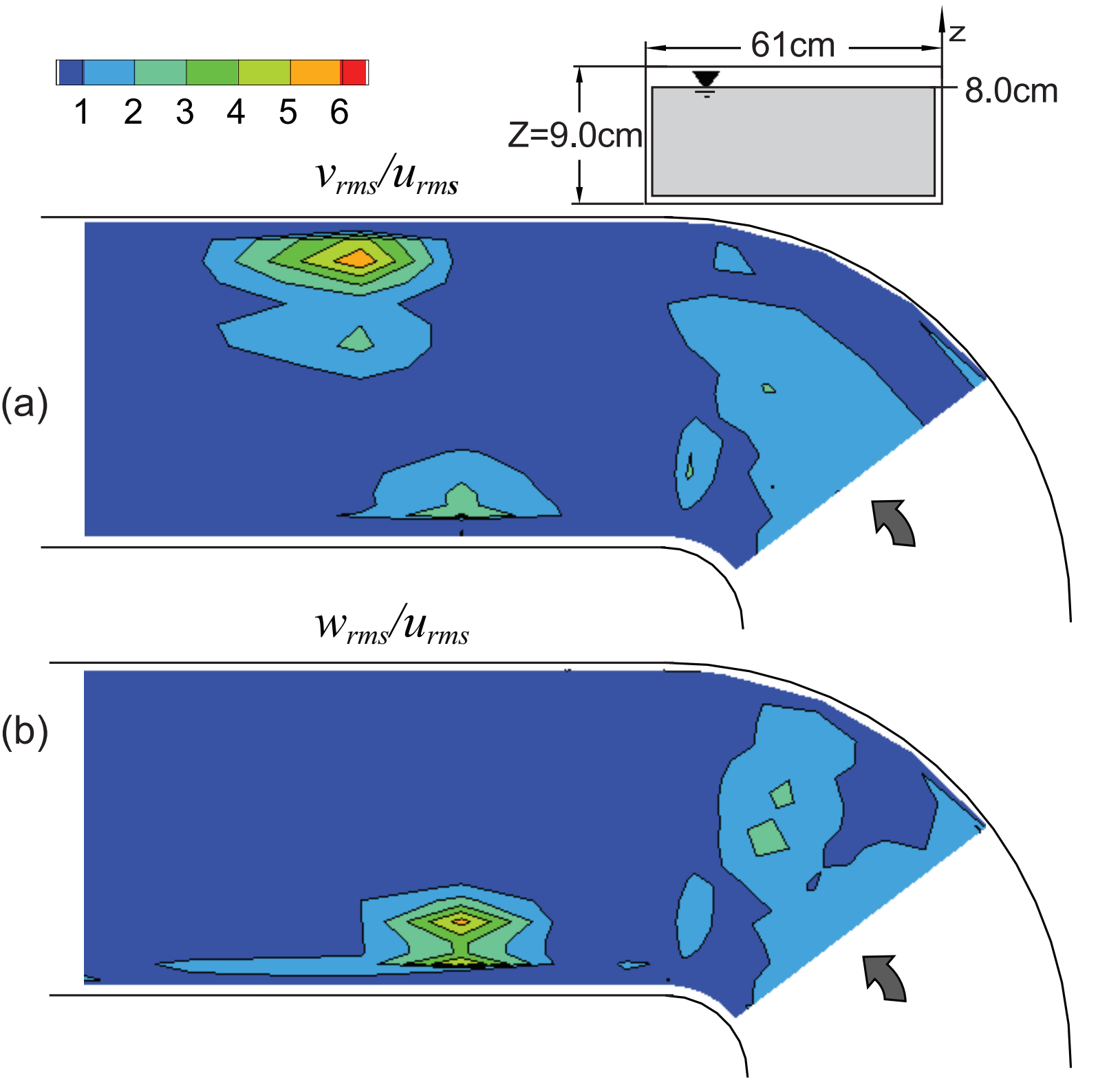


**Fig. 8.** Comparison of the ratio of root-mean square (rms) values of the velocity fluctuations at  $z/Z = 0.88$ : (a)  $v_{rms}/u_{rms}$ ; (b)  $w_{rms}/u_{rms}$

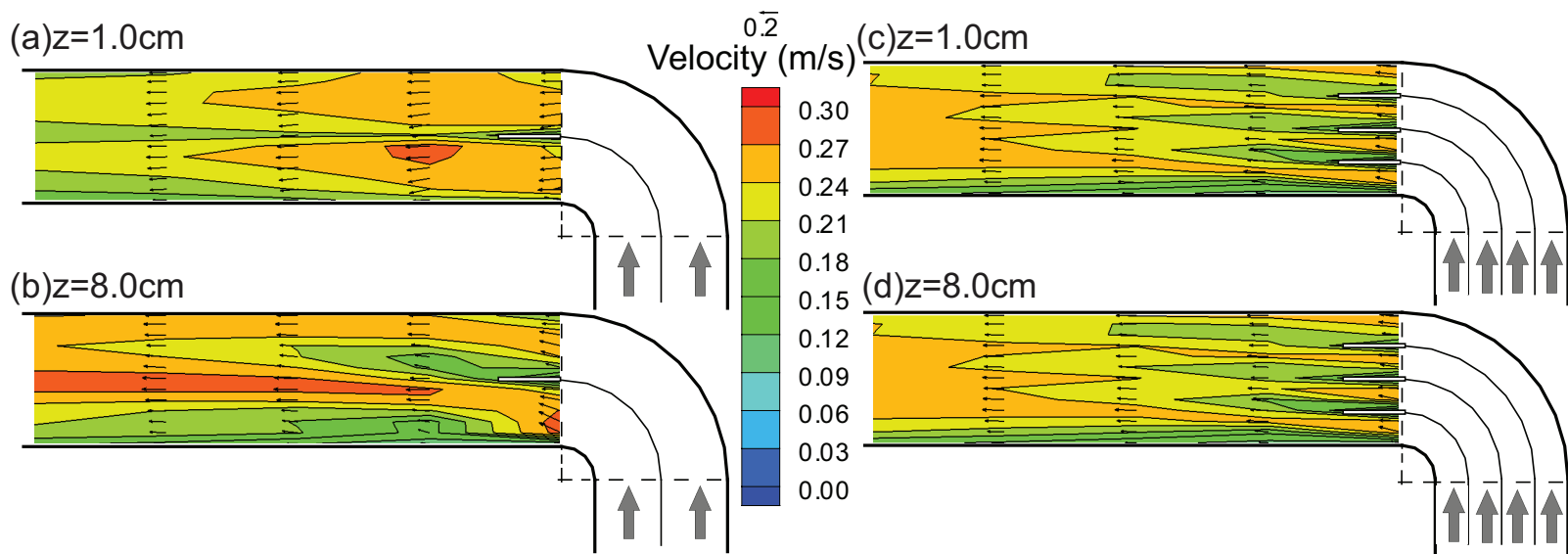


**Fig. 9.** Contours and vector plots of velocity for the downstream cross-sections of the bend with 1 vane at a)  $z/Z=0.11$  and b)  $z/Z=0.88$ , and with 3 vanes at c)  $z/Z=0.11$  and d)  $z/Z=0.88$ .

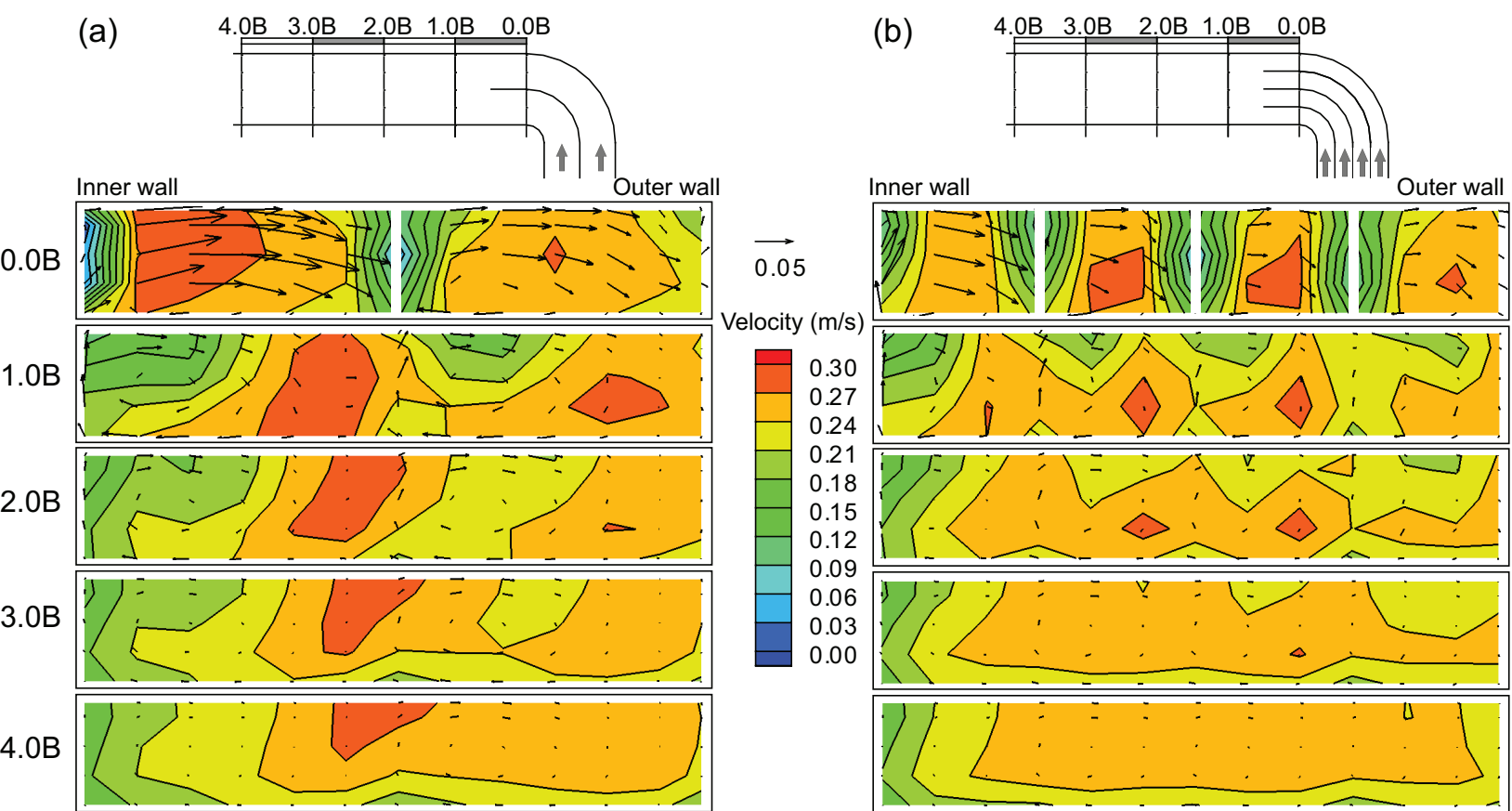


**Fig. 10.** Velocity magnitude with superimposed lateral and vertical velocity vectors at  $x_d/B = 0.0, 1.0, 2.0, 3.0, 4.0$  looking downstream for the configuration with: (a) 1 vane; (b) 3 vanes.

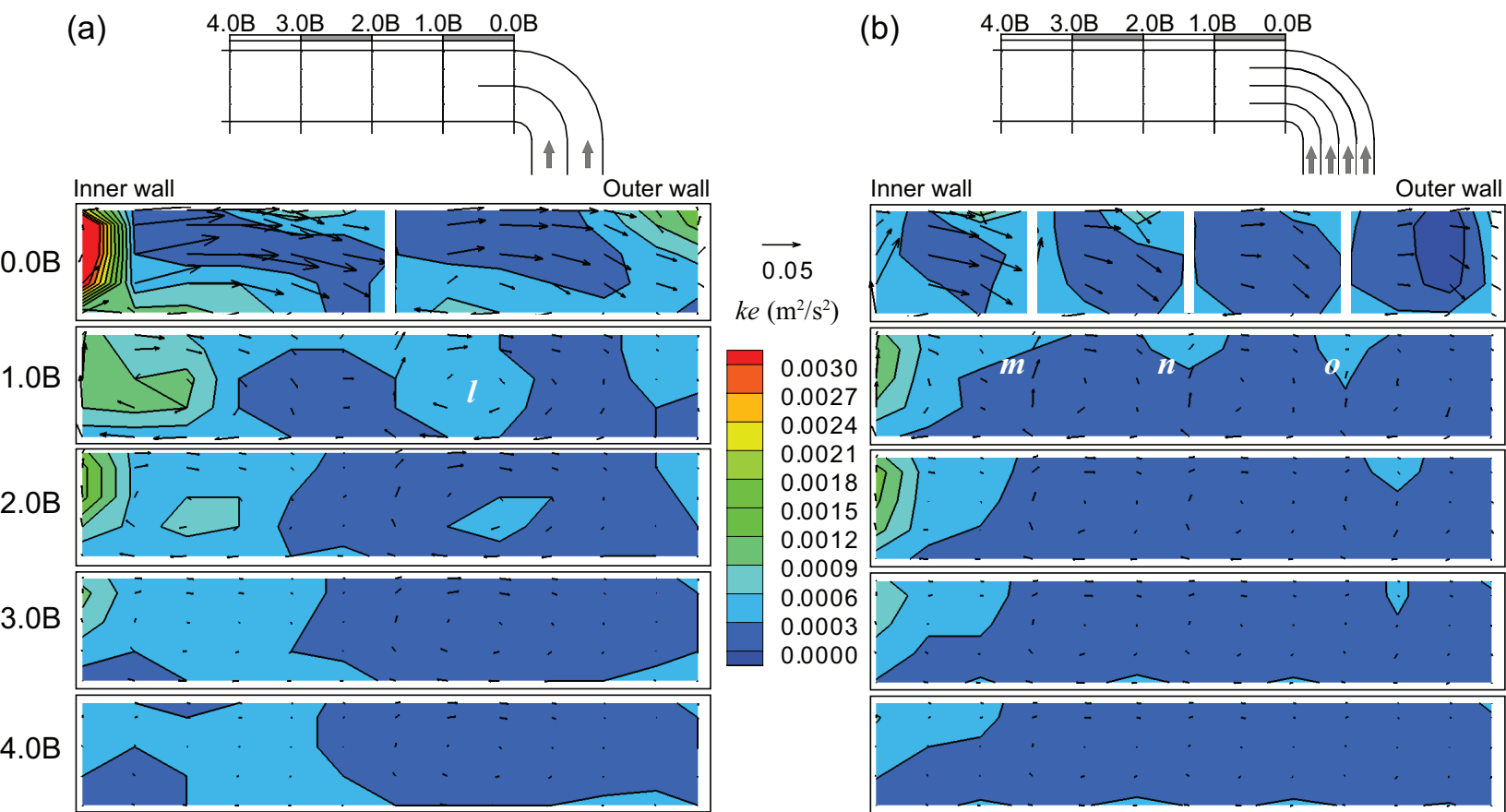


**Fig. 11.** Turbulent kinetic energy ( $ke$ ) with superimposed lateral and vertical velocity vectors at  $x_d/B = 0.0, 1.0, 2.0, 3.0, 4.0$  looking downstream for the configuration with: (a) 1 vane; (b) 3 vanes. Letters  $l, m, n, o$  represent pockets of high turbulence associated with each vane.

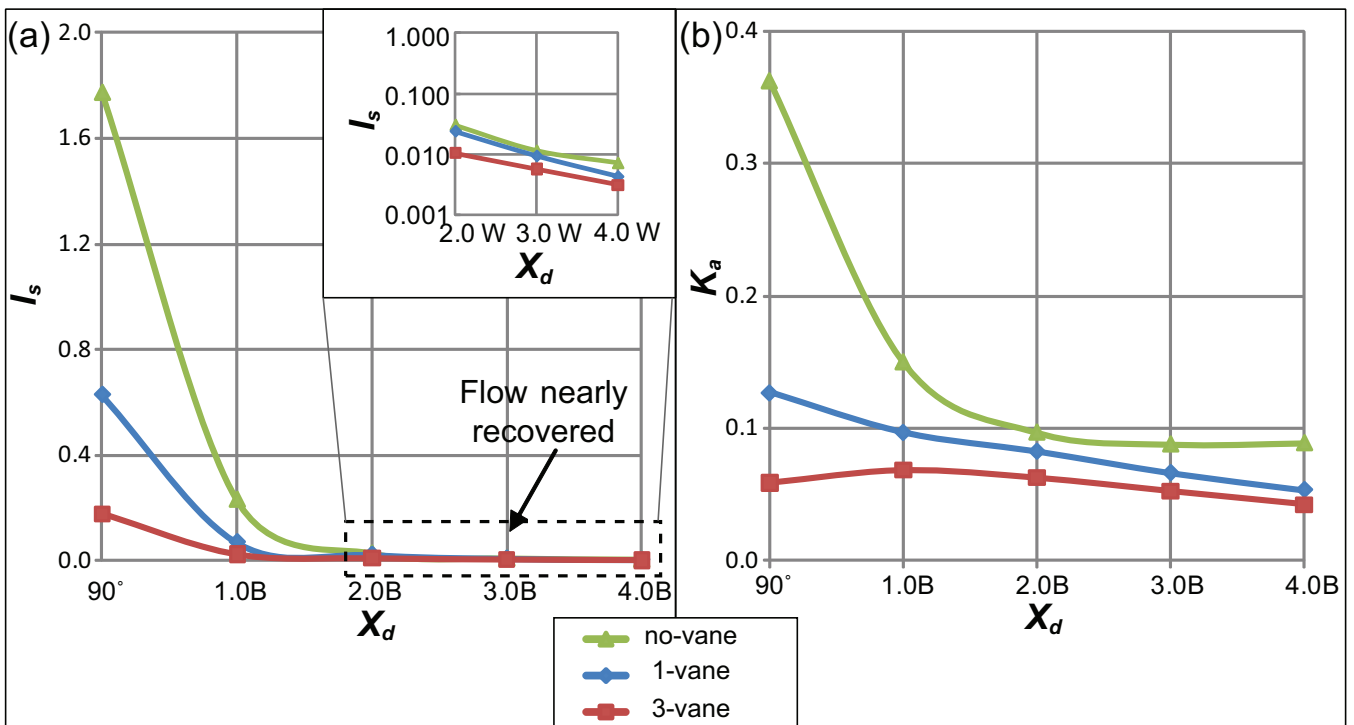


**Fig.12.** Cross-sectional average values of  $I_s$  and  $K_a$  along downstream channel for the bend configuration with and without vanes: (a)  $I_s$ ; (b)  $K_a$ . Insert: Details of  $I_s$  for range  $2.0 \leq x_d/B \leq 4.0$ .

**Fig. 1.** (a) Layout of the flume (dimensions are in meters); zoomed bend and downstream sections with the position of the measured cross sections (distances based on the width ( $B=0.61$  m)) for the configurations using (b) 1 vane; (c) 3 vanes.

**Fig. 2.** (a) Planform positions for LDA velocity measurements; (b) measuring points for no-vane system.

**Fig. 3.**  $U$ - $V$  vectors overlaid on contour plots of  $U_T$

**Fig. 4.** Water surface profiles at inner (blue squares) and outer (black triangles) walls with average water depth (red diamonds) and specific energy (green circles). Bend locations are in terms of  $\theta$  and channel locations are in terms of  $B$

**Fig. 5.** Measured water surface level fluctuations at  $0.1 B$  downstream of the bend: (a) outer wall; (b) middle of channel; (c) inner wall

**Fig. 6.** Vector plots of lateral and vertical velocity superimposed on contours of velocity magnitude (looking downstream) in the bend cross-sections at positions: (a)  $37.5^\circ$ ; (b)  $67.5^\circ$ ; (c)  $90^\circ$ ; and in the downstream channel at cross-sections (d)  $0.13B$  ( $=8$  cm); (e)  $0.64B$  ( $=39$  cm); (f)  $1.48B$  ( $=90$  cm) and (g)  $1.81B$  ( $=110$  cm).

**Fig. 7.** Contour plots of turbulent kinetic energy ( $ke$ ) at dimensional heights above bed ( $z/Z$ ) of a)  $0.07$ , b)  $0.50$  and c)  $0.88$ .

**Fig. 8.** Comparison of the ratio of root-mean square (rms) values of the velocity fluctuations at  $z/Z = 0.88$ : (a)  $v_{rms}/u_{rms}$ ; (b)  $w_{rms}/u_{rms}$

**Fig. 9.** Contours and vector plots of velocity for the downstream cross-sections of the bend with 1 vane at a)  $z/Z=0.11$  and b)  $z/Z=0.88$ , and with 3 vanes at c)  $z/Z=0.11$  and d)  $z/Z=0.88$ .

**Fig. 10.** Velocity magnitude with superimposed lateral and vertical velocity vectors at  $x_d/B = 0.0, 1.0, 2.0, 3.0, 4.0$  looking downstream for the configuration with: (a) 1 vane; (b) 3 vanes.

**Fig. 11.** Turbulent kinetic energy ( $ke$ ) with superimposed lateral and vertical velocity vectors at  $x_d/B = 0.0, 1.0, 2.0, 3.0, 4.0$  looking downstream for the configuration with: (a) 1 vane; (b) 3 vanes. Letters l, m, n, o represent pockets of high turbulence associated with each vane.

**Fig. 12.** Cross-sectional average values of  $I_s$  and  $K_a$  along downstream channel for the bend configuration with and without vanes: (a)  $I_s$ ; (b)  $K_a$ . Insert: Details of  $I_s$  for range  $2.0 \leq x_d/B \leq 4.0$ .